Transient Attracting Profiles in the Great Pacific Garbage Patch

Luca Kunz[1], Alexa Griesel[1], Carsten Eden[1], Rodrigo Duran[2,3], and Bruno Sainte-Rose[4]

[1]Institute of Oceanography, Universität Hamburg, Hamburg, Germany
[2]National Energy Technology Laboratory, U.S. Department of Energy, Albany OR, USA
[3]Theiss Research, La Jolla CA, USA
[4]The Ocean Cleanup, Rotterdam, The Netherlands

Correspondence: Luca Kunz (luca.kunz@uni-hamburg.de)

Abstract. A major challenge for cleanup operations in the Great Pacific Garbage Patch is the daily prediction of plastic concentrations that allows to identify hotspots of marine debris. Lagrangian simulations of large particle ensembles are the method in use and effectively reproduce observed particle distributions at synoptic scales $\mathcal{O}(1000\text{km})$. However, they lose accuracy at operational scales $\mathcal{O}(1-10\text{km})$ and operators regularly experience differences between predicted and encountered debris

5 accumulations within the garbage patch. Instead of asking *Where do objects go as they follow the current?* as in Lagrangian methods, we here take a different approach and question *Which locations attract material?*. The recently developed concept of Transient Attracting Profiles (TRAPs) provides answers to this since it allows to detect the most attractive regions of the flow. TRAPs are the attractive form of hyperbolic Objective Eulerian Coherent Structures and can be computed from the instantaneous strain field on the ocean surface. They describe flow features that attract drifting objects and could facilitate offshore

10 cleanups which are currently taking place in the Great Pacific Garbage Patch. However, the concept remains unapplied since little is known about the persistence and attractive properties of these features in the Pacific. Therefore, we compute a 20-years dataset of daily TRAP detections from satellite-derived mesoscale velocities within the North Pacific subtropical gyre. We are the first to track these instantaneous flow features as they propagate through space and time. This allows us to study the life cycle of TRAPs which can range from days to seasons and on average lasts for $\overline{\Lambda} \approx (6 \pm 12)$ days. We show how long-living

15 TRAPs with lifetimes of $\Lambda > 30$ days intensify and weaken over their life cycle and demonstrate that the evolution stage of TRAPs affects the motion of nearby surface drifters. Our findings indicate that operators in the Great Pacific Garbage Patch should search for long-living TRAPs that are at an advanced stage of their life cycle. These TRAPs are most likely to induce large-scale confluence of drifting objects and their streamlining into hyperbolic pathways. Such a streamlined bypass takes on average $\overline{\varphi} \approx (5.3 \pm 3.8)$ days and could be exploited to filter the flow around TRAPs. But we also find TRAPs that retain

20 material over multiple weeks where we suspect material clustering at the submesoscale, prospective research could investigate this with soon available high-resolution observations of the flow. Eventually, our research may also benefit other challenges that are related to the search at sea, such as optimal drifter deployment, the identification of foraging hotspots or humanitarian search and rescue.

25 **Short summary**

TRansient Attracting Profiles (TRAPs) indicate the most attractive regions of the flow and have the potential to facilitate offshore cleanup operations in the Great Pacific Garbage Patch. We study the characteristics of TRAPs and the prospects for predicting debris transport from a mesoscale permitting dataset. Our findings provide an advanced understanding of TRAPs in this particular region and demonstrate the importance of TRAP lifetime estimations to an operational application. Our algorithm
30 to track TRAPs complements the recently published TRAPs concept and prepares its use with high-resolution observations from the SWOT mission. Our findings may also benefit research in other fields like e.g. optimal drifter deployment, sargassum removal, the identification of foraging hotspots or search and rescue.

1 Introduction

The horizontal long-term flow at the ocean surface is understood as the main forcing that transports floating material over large distances (van Sebille et al., 2020) and can be well-described by the combination of geostrophic and Ekman currents (Röhrs et al., 2021). Floating marine debris follows the large-scale convergence within each of the five subtropical gyres and forms basin-scale accumulation zones (van Sebille et al., 2020) which exhibit elevated levels of plastic concentration. In this context, the North Pacific subtropical gyre is to date the area of highest scientific and public concern. First initiatives to clean up ocean plastic pollution at global scale are taking place in this particular gyre (Slat, 2022) and a variety of experiments has been dedicated to estimating the limits of this accumulation zone which is colloquially termed the *Great Pacific Garbage Patch* (Onink et al., 2019; Lebreton et al., 2018; Law et al., 2014). Figure 1 highlights this large-scale convergence zone and the horizontal long-term flow at the surface of the northeast Pacific ocean.
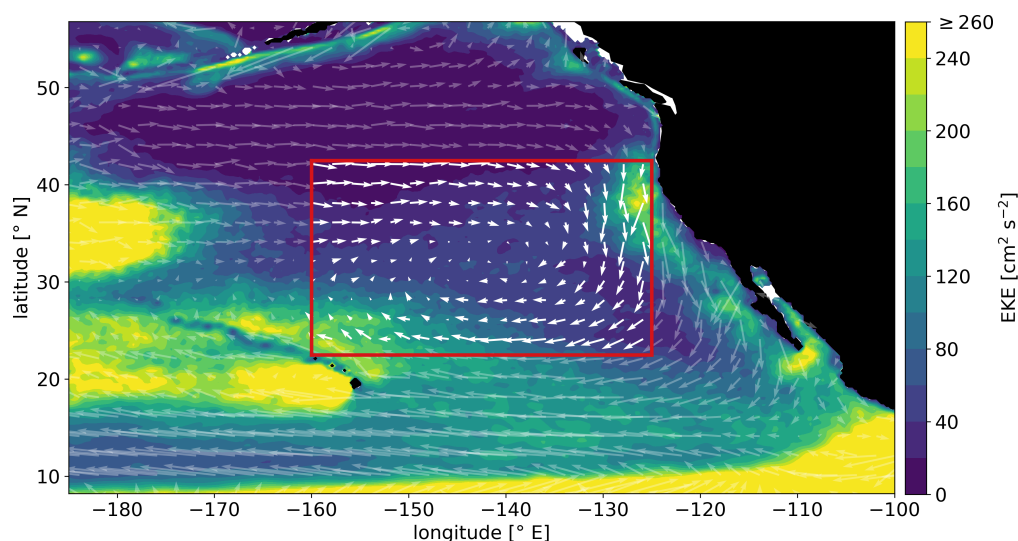
Figure 1. Mean circulation and EKE in the eastern North Pacific. Quivers indicate the direction and magnitude of 20-years average near-surface geostrophic + Ekman current velocities for the period 2000-2019 (CMEMS, 2022a). Arrow size scales with increasing velocity magnitude, the red box defines our study domain and highlights the area of large-scale convergence due to Ekman transport. In this region, the Great Pacific Garbage Patch is expected to be located (Law et al., 2014; Lebreton et al., 2018; Onink et al., 2019). The ocean surface is coloured by the magnitude of eddy kinetic energy (EKE) w.r.t. to the same period, derived from geostrophic currents only (CMEMS, 2022b).

A constant challenge for cleanup operations in this region is to predict day to day variabilities of plastic concentrations and with this identify hotspots of marine debris. The common method is to release large ensembles of virtual particles at the ocean surface and to derive their trajectories and distribution as they follow the time-evolving surface flow (van Sebille et al., 2018; van Sebille et al., 2020; Duran et al., 2021). Measurements from altimetry or estimations from numerical ocean models typically provide the velocity fields that drive these Lagrangian particle simulations which eventually allow to derive particle

concentrations at the ocean surface. At synoptic scales $\mathcal{O}(1000\mathrm{km})$, Lagrangian simulations succeed in predicting the limits

50 of the Great Pacific Garbage Patch (Onink et al., 2019; Lebreton et al., 2018; Law et al., 2014). However, within the garbage patch and at operational scales $\mathcal{O}(1-10\mathrm{km})$, The Ocean Cleanup reports that Lagrangian simulations often fail in accurately predicting the particle distributions they observe at sea. This deficiency can be a consequence of the combination of Lagrangian methods with submesoscale velocity estimations from numerical models. At operational scales and within this region, numerical models currently represent the only source for now- and forecast estimations of the surface flow, but these simulations can

55 only approximate the true dynamics at sea. On the other hand, Lagrangian simulations can produce significant trajectory errors if the underlying velocity data or the trajectory modeling itself are missing important physics and errors accumulate quickly during the integration process (Duran et al., 2021).

Instead of asking *Where do objects go as they follow the current?* as in Lagrangian methods, we here take a fundamentally

60 different approach and question *Which locations attract material?*. The recently published concept of Transient Attracting Profiles (TRAPs, Serra et al. (2020)) provides answers to this since it allows to detect the most attractive regions of the flow. TRAPs are the attractive form of hyperbolic Objective Eulerian Coherent Structures (OECSs, Serra and Haller (2016)) and can be computed from the symmetric part of the velocity gradient. They indicate regions of maximal compression and stretching on the ocean surface which are expected to translate into the attraction and hyperbolic transport of nearby floating objects.

65

Serra et al. (2020) and Duran et al. (2021) provide experiments that show the capability of TRAPs to attract drifting objects. They demonstrate how TRAPs uncover stretching of tracer patterns that is hidden to conventional diagnostics like streamlines or divergence. Their experiments also indicate that TRAPs are insensitive to the shape, submergence level, release time and release position of drifting objects. These parameters are generally uncertain in applications but must be considered in La-

70 grangian simulations. Moreover, Serra and Haller (2016), Serra et al. (2020) and Duran et al. (2021) argue that TRAPs are more robust to moderate errors in the underlying velocity field while trajectory-based methods are sensitively dependent to inevitable errors, see Table B1 for more benefits.

So it stands to reason that TRAPs could facilitate offshore cleanups which are currently taking place in the Great Pacific

75 Garbage Patch. However, the concept remains unapplied since the persistence and attractive properties of TRAPs have not been characterised in this particular region. Therefore, we create a 20-years dataset of daily TRAP detections and study these features within the North Pacific subtropical gyre.

We compute TRAPs from near-surface geostrophic + Ekman current velocities since geostrophic velocity from altimetry is

80 the only large-scale observation that resolves flow features at the mesoscale (Abernathey and Haller, 2018). Many studies have established that altimetry-derived velocity products are accurate for Lagrangian transport applications, see e.g. Sect. 3.1.3 of Duran et al. (2021) and references therein. Moreover, the contributions we make can be applied to higher-resolution observa-

tions that soon will be available from the SWOT mission (International Altimetry Team, 2021).

Since altimetry can be seen as a filter for the ocean circulation that seperates out all small-scale, short-term features of the flow, our study is naturally embedded in the low-frequency circulation. This motivates us to locate TRAPs within the mesoscale eddy field by comparing our dataset to corresponding records of mesoscale eddy detections. We investigate how these coherent structures relate in order to advance our understanding of strain between eddies and how it can be utilised to predict debris transport.

TRAPs that persist over several days will then highlight permanent features of the flow where we might find large-scale confluence of material. The detection of persistent TRAPs can therefore help to point cleanup operations in the right direction which motivates us to design a tracking algorithm that follows TRAPs through space and time. We are the first to track these Eulerian flow features, to determine their lifetimes and to describe their propagation through the domain. We further combine these findings with observations of surface drifters to investigate the TRAP properties that are relevant for an offshore cleanup in the Great Pacific Garbage Patch. But the findings we make also have the potential to facilitate maritime search operations in other contexts and regions.

The paper is organised as follows. In Section 2 we review the theoretical aspects of Transient Attracting Profiles, outline the design of the experiment and go through the methods we use to give a comprehensive analysis of mesoscale TRAPs. Section 3 presents the results of our analysis in four parts - the spatial distribution of TRAPs, their life cycle and propagation, vorticity patterns around TRAPs and the impact of TRAPs on nearby drifters. In Section 4 we discuss our findings and the directions they offer for future research.

2 Methodology

2.1 Transient Attracting Profiles

Serra et al. (2020) derive TRAPs from the instantaneous strain field of the ocean surface using snapshots of the two-dimensional surface velocity field $\boldsymbol{u}(\boldsymbol{x}, t)$. The symmetric part of the velocity gradient represents the time-dependent strain tensor $\mathbf{S}(\boldsymbol{x}, t) = \frac{1}{2}(\boldsymbol{\nabla}\boldsymbol{u}(\boldsymbol{x}, t) + [\boldsymbol{\nabla}\boldsymbol{u}(\boldsymbol{x}, t)]^\top)$ with eigenvalues s_i and eigenvectors $\boldsymbol{e}_i$. We apply the notation for the diagonal form of $\mathbf{S}(\boldsymbol{x}, t)$ from Serra and Haller (2016):

$$\mathbf{S}\boldsymbol{e}_i = s_i\boldsymbol{e}_i, \quad |\boldsymbol{e}_i| = 1, \quad i = 1, 2; \quad s_1 \leq s_2, \quad \boldsymbol{e}_2 = \mathbf{R}\boldsymbol{e}_1, \quad \mathbf{R} := \begin{pmatrix} 0 & -1 \\ 1 & 0 \end{pmatrix} \tag{1}$$

The deformation of any fluid's surface element A is determined by the strain rates s_i which specify the rates of stretching ($s_i > 0$) or compression ($s_i < 0$) of A along the principle axes indicated by the eigenvectors $\boldsymbol{e}_i$, see (Olbers et al., 2012) for details. Due to $s_1 \leq s_2$, $\boldsymbol{e}_1$-lines describe lines of minimal and $\boldsymbol{e}_2$-lines lines of maximal stretching for a non-uniform deformation. The compression and stretching of surface elements translates into the attraction and repulsion of material and negative local minima of $s_1(\boldsymbol{x}, t)$ therefore describe the most attractive regions of the flow, maximising attraction normal to $\boldsymbol{e}_2$. For incompressible conditions, $s_1 = -s_2$ further holds and local minima of s_1 simultaneously indicate local maxima of s_2, so that the strongest attraction and strongest repulsion then occur at the same position and in orthogonal directions.

TRAPs represent $\boldsymbol{e}_2$-lines starting at negative local minima of the s_1 strain field and extend until s_1 along the $\boldsymbol{e}_2$-line ceases to be monotonically increasing. Consequently, TRAPs contain one minimum value of s_1, i.e. the point of strongest attraction perpendicular towards the TRAP. The position of this minimum value is called the TRAP *core* which represents an objective saddle-type stagnation point of the unsteady flow (Serra and Haller, 2016). The TRAP itself, as it is at every point tangent to the unit eigenvector $\boldsymbol{e}_2$ describes the direction of maximum stretching and will in the following also be referred to as TRAP *curve*.

Figure 2 shows an example of a Transient Attracting Profile. The TRAP is displayed as a red curve with the TRAP core as red dot in the middle. The image displays this structure upon a colourmap of the underlying s_1 strain field as well as velocity quivers derived from the same snapshot of surface geostrophic + Ekman current velocity. The TRAP core is positioned in the point of highest attraction, i.e. a negative local minimum of the s_1 field, and the velocity vectors indicate the flow around the TRAP, i.e. water motion normal towards the TRAP and subsequent transport to both ends of the structure. The figure also displays the positions of this TRAP after 10 and 20 days.
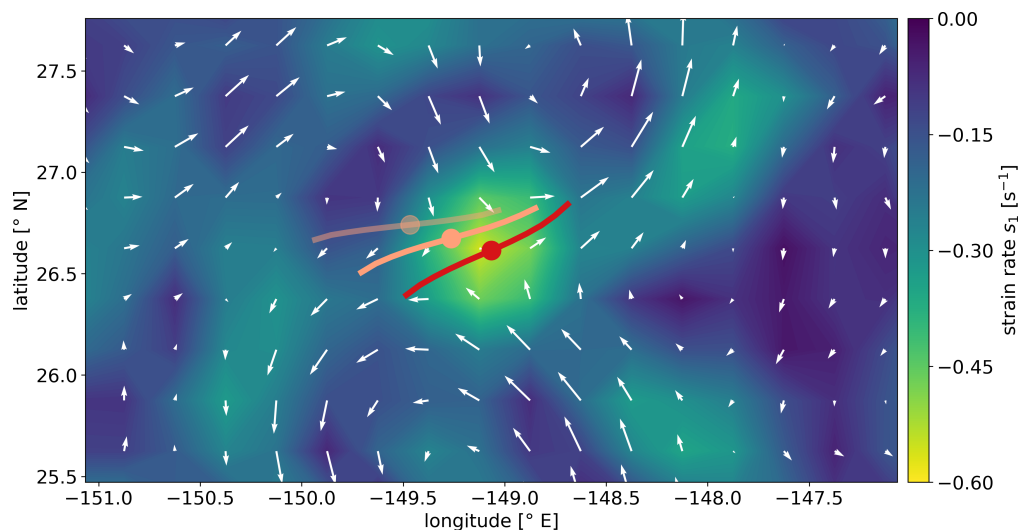
Figure 2. Example Transient Attracting Profile. The red structure represents one TRAP from our 20-years record of daily TRAPs, computed from snapshots of surface geostrophic + Ekman current velocity (CMEMS, 2022a). The red dot in the middle indicates the TRAP core, the red line the TRAP curve. Quivers illustrate the flow around the structure and the colourmap indicates the s_1 strain field derived from the same velocity snapshot. The geometries in salmon colour indicate with increasing transparency the position of the same TRAP after 10 and 20 days.

2.2 TRAPs computation

135   Serra et al. (2020) have published a programme to compute TRAPs from two-dimensional snapshots of a Eulerian velocity field $u(x,t)$ (Serra, 2020), see Table B2 for details of the algorithm and Kunz (2024a) , Kunz (2024b) for our post-processing of the output. We set TRAPs to a maximal arclength of 1° to represent a reasonable length scale for the regions between mesoscale eddies that is at the same time representative for cleanup operations. We call the points that discretise the TRAP curve *curve points* and the programme gives the positions of all curve points and corresponding TRAP cores in the domain.

140   It further outputs the normal attraction rate s_1 at every TRAP core, which we name *core attraction*. We set the boundaries of our study domain to [22.5° N, 42.5° N] in latitudes and [-160° E, -125° E] in longitudes and compute TRAPs within this domain. We choose these limits, highlighted by the red box in Fig. 1, in order to enclose the North Pacific accumulation zone between Hawaii and California as defined by Onink et al. (2019). These boundaries also warrant no intersection with any land mass. We compute TRAPs from daily snapshots of near-surface geostrophic + Ekman currents and therefore extract the

145   velocity fields *uo* and *vo* from the product *Global Total Surface and 15m Current (COPERNICUS-GLOBCURRENT) from Altimetric Geostrophic Current and Modeled Ekman Current Reprocessing* that is provided by the E.U. Copernicus Marine Service (CMEMS, 2022a). The velocity fields are available at three-hourly instantaneous time steps, from which we select data at UTC midnight to sample snapshots with a daily frequency. Velocity fields are provided on a latitude-longitude grid of 0.25° resolution.

150

2.3 Tracking Algorithm

Our tracking algorithm runs on the full TRAPs record and finds spatially proximate detections at consecutive timestamps which can be identified as one single feature of the flow. The only free parameter ϵ defines the size of the search area around a current TRAP to look for a detection in the next snapshot and is set to $\epsilon = 0.25°$, see Kunz (2024a) for more details. The

155 algorithm assigns a unique label to each TRAP trajectory and its associated instances and it derives metrics like e.g. the lifetime Λ of TRAPs and their age τ at a particular snapshot. We can then derive the zonal and meridional translation speeds c_x and c_y for every instance of a TRAP trajectory. Therefore we choose all TRAPs that persist for at least three days and average the forward and backward shifted velocity at a current timestamp. The forward/backward shifted velocity is the distance to its succeeding/preceding position divided by the time lapsed between both instances, respectively. This way we deliberately create

160 no velocities at the start and end of a trajectory and do not gain propagation speeds for trajectories of two days lifetime. In turn, we obtain translation speeds of individual TRAP instances which we consider more accurate than taking the full distance travelled by a TRAP and dividing it by the respective lifetime.

2.4 Mesoscale eddy data

We compare TRAPs against eddy detections from The altimetric Mesoscalle Eddy Trajectory Atlas (META3.2 DT) which is
165 produced by SSALTO/DUACS and distributed by AVISO+ with support from CNES, in collaboration with IMEDEA (AVISO+ et al., 2022). This dataset provides Eulerian detections of eddies derived from sea surface height (SSH) contours, is at frequency with our TRAPs record and includes estimations of the eddy contour speed U. The eddy contour speed U is the average geostrophic speed of the contour of maximum circum-average geostrophic speed for the detected eddy. We filter the dataset for eddy detections within the study domain and period and retrieve 28,645 cyclonic and 24,193 anticyclonic eddy trajectories
170 from 689,460 cyclonic and 686,720 anticyclonic eddy detections. Since we simply cut off eddy trajectories beyond the domain boundaries, 4.2% of all eddy trajectories will show discontinuities since they leave and return into the domain. We do not correct for this cut off since the impact on our aggregate statistics should be negligible. We estimate eddy lifetime by taking the difference between the first and the last occurrence within our domain, added by one day. As a consequence, the estimated eddy lifetime can also include times spent outside the domain, given that the eddy returns back into it again. We further derive
175 eddy propagation speeds as we do for TRAPs.

2.5 Vorticity curve

We use the relative vorticity field to characterise the flow around TRAPs. Many TRAPs seem to be surrounded by four vortices of alternating polarity. In this case, two vortices on each side of a TRAP curve exhibit perpendicular flow towards the TRAP core and tangential flow away from it, with respect to the TRAP curve. We call this vorticity pattern a *quadrupole* and classify
180 variations of it. To detect vorticity patterns without a coordinate transformation, we draw a circle in the horizontal plane around every TRAP core with a radius equal to the distance between the core and the furthest curve point. Starting from the position of the furthest curve point, we parameterize the circle with angles increasing counter-clockwise, and bilinearly interpolate the

vorticity field to the points on this circle. The *vorticity curve* $\zeta(\alpha)$ then describes the vorticity along this circle with respect to the angle of parameterisation, i.e. the phase α.

185

By visualising the vorticity curve, we are able to directly see polarity changes in the surrounding vorticity field and their spatial orientation towards the TRAP. Figure 3a illustrates an example of such a vorticity measurement around a TRAP. For a quadrupole in the northern hemisphere, the polarity pattern along the vorticity curve then results in cyclonic ($\oplus$, positive vorticity), anticyclonic ($\ominus$, negative vorticity), cyclonic, anticyclonic and the vorticity curve reveals four zero crossings.

190

Since the ensemble mean of all vorticity curves $\zeta(\alpha)$ indicates a quadrupole pattern, we filter the ensemble for specific combinations of four vortices of either cyclonic or anticyclonic rotation. We do not explicitly resolve patterns with less than four vortices because we can identify them from this classification if needed. In total, there are 2^4 possible vortex combinations, 10 of which exert distinct dynamics, i.e. are unique under rotations of 180° around a TRAP core. To isolate each pattern, we

195 further remove a constant average background vorticity from every vorticity curve and then filter the ensemble for these 10 vortex combinations. To detect the vortex configuration within a given vorticity curve, we divide the curve into four phase intervals of $\alpha_I = [0, \pi/2)$, $\alpha_{II} = [\pi/2, \pi)$, $\alpha_{III} = [\pi, 3\pi/2)$, $\alpha_{IV} = [3\pi/2, 2\pi)$ and compute the average vorticity within each interval, see Fig. S2 for more details on all 10 vorticity patterns.
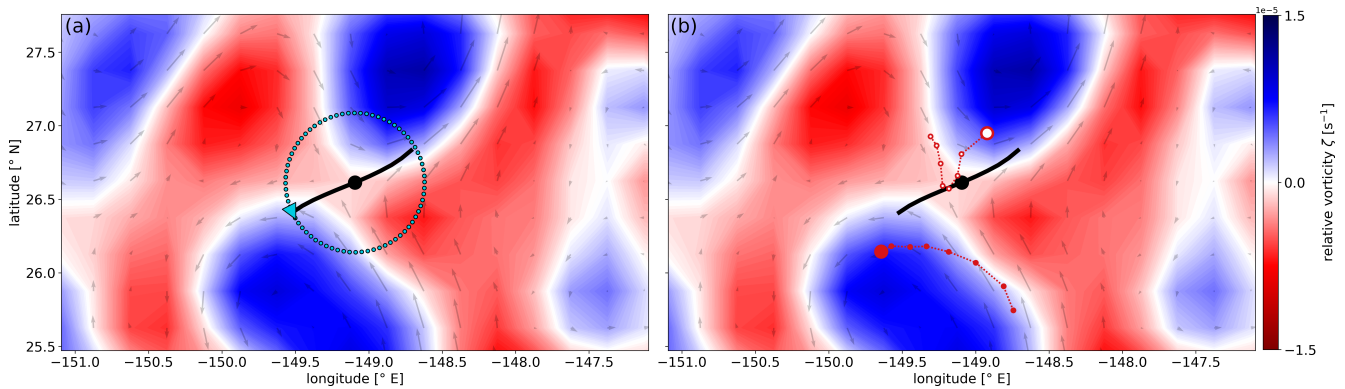
Figure 3. Vorticity circle and drifter transport around a TRAP. (a) For each TRAP, the vorticity field ζ is interpolated to points on a circle around the core (dotted line). The circle parameterisation starts at the position of the furthest curverpoint w.r.t. the core (triangle) and with a phase of $\alpha = 0°$. α increases counter-clockwise and we sample the vorticity along the curve as vorticity curve $\zeta(\alpha)$. (b) Filled and empty big red circle markers indicate the current position of one drogued and one undrogued drifter around the same TRAP instance, respectively. Red tails with small markers indicate their positions throughout the preceeding seven days. Quivers illustrate the surrounding flow and the colourmap indicates the relative vorticity field ζ.

2.6 Impact on drifters

Since TRAPs highlight the most attractive regions and their cores represent objective saddle points of the unsteady surface flow, we expect them to attract and disperse drifting objects in a hyperbolic pattern. We study their transient impact on drifting objects and therefore look at surface drifter trajectories around TRAPs.

To compare drifters and TRAPs at simultaneous timestamps, we consult 24-hourly drifter positions at UTC midnight from the Global Drifter Program (Lumpkin and Centurioni, 2019). For our study domain and period, this dataset provides 842, i.e. 328 drogued and 514 undrogued, drifter trajectories distributed over 221,979, i.e. 67,885 drogued and 154,094 undrogued, positions. We call these daily drifter positions *drifter days*. Figure 3b illustrates an example for hyperbolic drifter motion that we find in this dataset - drifters are first attracted perpendicular towards the TRAP and then transported along one of its branches towards the end. This is how TRAPs are expected to organise nearby floating objects. See Fig. S1 in the Supplementary Material for an overview on all drifter positions.

We want to see how drifters behave in the surroundings of a TRAP and therefore detect pairs of drifters and nearby TRAPs. In Kunz (2024a) we provide a comprehensive description of our pair algorithm that works from a drifter's perspective and searches for the closest TRAP within a distance of 75 kilometres. For every instance of a drifter-TRAP pair, the algorithm records the drifter's distance to the closest TRAP. It also saves attributes like e.g. the TRAP age τ at first encounter, the TRAP lifetime Λ and its attraction rate s_1. Moreover, we will know the daily vorticity pattern in which a drifter-TRAP pair is embedded, and we measure the pair's duration, i.e. the retention time φ of a drifter around its closest TRAP. A lot of pairings will only last for a day due to ephemeral TRAPs with $\Lambda = 1$ day, due to drifters passing by in the periphery of a TRAP or due to the drifter finding another TRAP that is closer. We exclude these one-day pairs from our analysis since we cannot infer any motion statistics from them. But the scope of our remaining measurements will still allow us to carry out a statistical analysis about drifter motion around TRAPs.

3 Results

3.1 Spatial distribution of TRAPs

We first look at important circulation features of the study area. Figure 1 shows the distribution of eddy kinetic energy (EKE) over the domain with respect to the period 2000-2019. The lowest values of EKE occur in the northwest corner of the domain. This subregion is part of an *eddy desert* in the northeast Pacific where mesoscale eddies are low in amplitude and short in lifetime, if present at all (Chelton et al., 2011). There are two distinct regions of high EKE in the northeast and the southwest of the domain, indicating frequent turbulence and mesoscale eddy activity. These two regions neighbour the California Upwelling System (CALUS) and the North Hawaiian Ridge Current (NHRC), respectively, which are known for the production of energetic mesoscale eddies (Pegliasco et al., 2015; Lindo-Atichati et al., 2020).

Within our domain and period, we detect 4,076,065 TRAP instances from which we identify 720,391 TRAP trajectories. TRAPs occur everywhere in the domain but with distinct patterns in quantity, persistence and attraction strength. In panel (a) of Fig. 4 we separate the domain into bins of $0.25° \times 0.25°$ and show the 20-year bin averages of instantaneous TRAP core attraction rates s_1. A comparison with Fig. 1 reveals that TRAPs are particularly strong in regions of high EKE close to the CALUS and the NHRC. In the central-north, the middle and southeast of the domain, moderate to low EKE prevails and TRAPs are on average moderately to weakly attracting. The eddy desert in the northwest corner remains with a clear preference for weak TRAPs. We derive a mean attraction rate and standard deviation of $\overline{s}_1 \approx (-0.23 \pm 0.11)$ s^{-1} over all TRAP instances. The most attractive TRAP that we find is located within the eastern hotspot of Fig. 4a and exhibits an attraction rate of $s_1 = -1.73$ s^{-1}. We correlate the average attraction rates s_1 from Fig. 4a with the EKE field given in Fig. 1 and find a pearson correlation coefficient of $r = -0.93$ with a p-value of $p < 0.001$. This indicates a strong and significant negative correlation between both variables. It suggests that weak/strong TRAPs, i.e. with a less/more negative attraction rate s_1, are located in regions of low/high EKE.

In panel (b) we visualise our tracking results and show the trajectories of TRAPs with lifetimes $\Lambda > 30$ days. We call this subset *long-living* TRAPs. From time lapse animations of the TRAPs field we suspect that the trajectories here indicate westward propagation with a tendency towards the equator, see Videos SV1, SV2 and SV3 in (Kunz, 2024c). Pegliasco et al. (2015) find similar propagation characteristics for anticyclonic mesoscale eddies that originate in the California Upwelling System east of our domain. A comparison to panel (a) suggests that attraction strength may vary along the trajectories of long-living TRAPs which however will exclude very weak attraction rates. Long-living TRAPs are indeed stronger than TRAPs with lifetimes $\Lambda \leq 30$ days. We find mean attraction rates of $\overline{s}_{1,\Lambda>30} \approx (-0.28 \pm 0.11)$ s^{-1} and $\overline{s}_{1,\Lambda\leq30} \approx (-0.20 \pm 0.09)$ s^{-1} for TRAP instances associated with these groups, respectively.

In panel (c) we separate the domain into bins of $1° \times 1°$ and count the number of TRAP trajectories that pass through each histogram bin. We find more TRAPs passing through the northwest than through the southeast half of the domain. TRAP

trajectories are especially abundant around the eddy desert, i.e. in the northwest and central-north of the study region. We complete the picture by deriving the average lifetime $\overline{\Lambda}$ of all trajectories that pass through a histogram bin in panel (d). We

260 find a clear preference for ephemeral TRAPs in the northwest corner and for persistent TRAPs within the southeast half of the domain. We summarise that TRAP trajectories are very abundant but only remain for a few days around the eddy desert while they become less abundant but more persistent towards the equator and the eastern boundary.
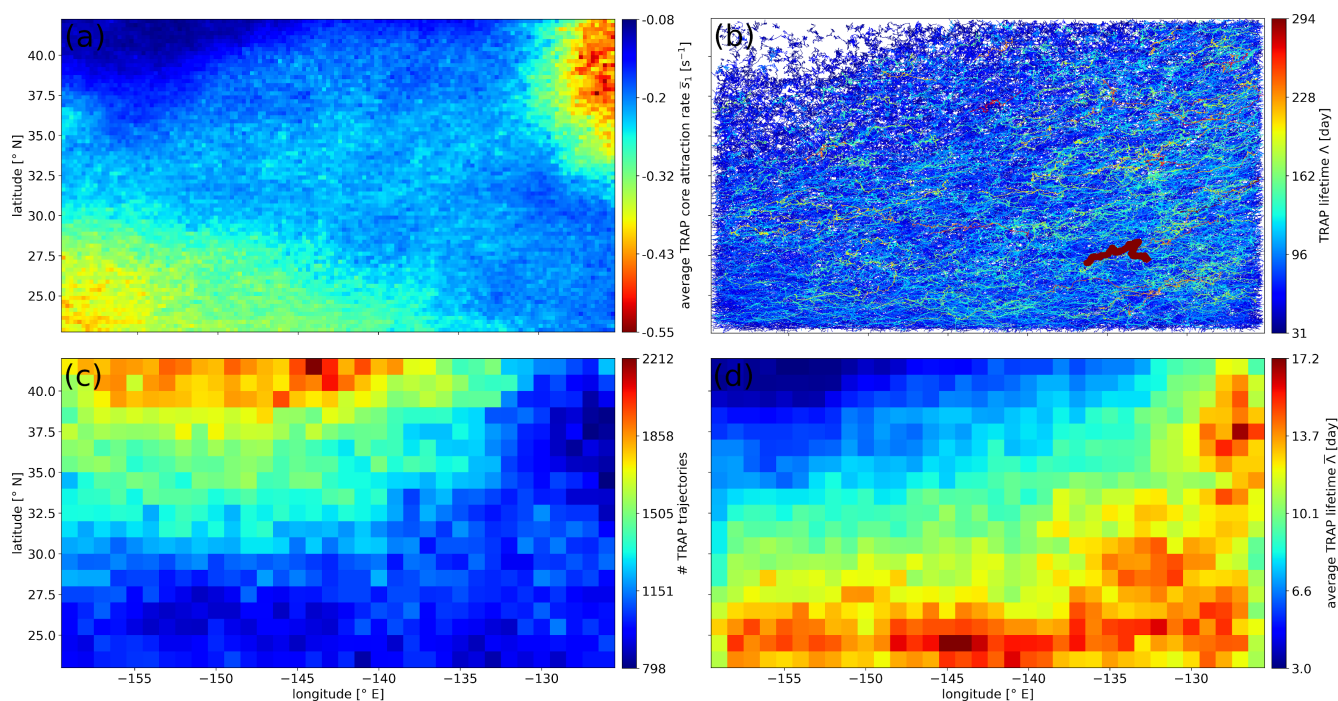
Figure 4. Distribution of TRAP characteristics over the domain and in the period 2000-2019. (a) TRAP core attraction strength s_1 averaged over 20 years and all instances within bins of $0.25° \times 0.25°$ size. Red colours indicate high attraction. (b) Trajectories of long-living TRAPs with lifetimes $\Lambda > 30$ days. Trajectories are coloured by the associated TRAP lifetime Λ, using the respective colour scale on the right. The most persistent TRAP is indicated by a thick line. (c) Number of identified TRAP trajectories that pass through histogram bins of $1° \times 1°$ size. (d) Average lifetime $\overline{\Lambda}$ of TRAP trajectories passing through each bin.

3.2 Life cycle and propagation

265 We find that TRAPs typically persist for a view days. However, the life cycle of some profiles can also span several seasons. Figure 5a presents the distribution of TRAP lifetimes Λ over all TRAP trajectories. We find a mean lifetime of $\overline{\Lambda} \approx (6 \pm 12)$ days. The most persistent TRAP counts a lifetime of $\Lambda = 294$ days and is indicated by the thick red-brown trajectory in Fig. 4b. Only 4% of all TRAP trajectories exhibit lifetimes of $\Lambda > 30$ days, but they include around 41% of all instantaneous detections.

270   In Fig. 5a we also present the lifetime distribution for mesoscale eddy detections in our domain. We consult the eddy census product by AVISO+ et al. (2022) to provide a first overview of three comparable features between TRAPs and mesoscale eddies. AVISO+ et al. (2022) identify 28,645 cyclonic and 24,193 anticyclonic mesoscale eddy trajectories within our study domain and period. On average, these cyclonic eddies persist for $\overline{\Lambda}_{\oplus} \approx (24 \pm 40)$ days and anticyclonic ones for $\overline{\Lambda}_{\ominus} \approx (29 \pm 56)$ days. The distributions in panel (a) resemble one another, but there are considerably more TRAP than eddy trajectories in our domain

275   and their lifetimes are shifted towards smaller values. Over their lifetime, approx. 25% of all TRAPs find no eddy detection, 54% find one and 21% find multiple eddy detections within a radius of $0.5°$ arclength. We find that this cumulative number of encounterd eddy detections depends on TRAP lifetime with a correlation coefficient of $r = 0.65$ and a p-value of $p < 0.001$. Long-living TRAPs encounter on average four eddy detections over their life cycle while some of them can be related to up to 18 different eddy detections. From this we understand that the detections from AVISO+ et al. (2022) are not really suitable to

280   explain individual TRAP detections.

We expect high rotation speeds of mesoscale eddies to create high strain between them which should reflect in a relation between s_1 and the eddy contour speed U. We investigate this relation by recasting panel (a) from Fig. 4 but for the mean eddy contour speeds U. We find a correlation coefficient between both histograms of $r = -0.94$ with a p-value of $p < 0.001$.

285   It confirms that on average, TRAP attraction strength scales with eddy contour speed. Panel (b) of Fig. 5 then views on the evolution of s_1 and U over the lifetime of long-living TRAPs and eddies. We adopt this approach from Pegliasco et al. (2015) who study the evolution of eddy radii and amplitudes. On average, both TRAP attraction and eddy contour speed intensify in the first half and decrease in the second half of a respective life cycle. We conclude that the life cycles of TRAPs and eddies relate.

290

Panel (c) presents the latitudinal dependence of the zonal translation speed c_x for TRAPs and eddies. We find that for both, c_x is primarily negative and thus westward. The mean values $\overline{c}_x$ vary with latitude and decrease towards the equator which indicates that both phenomena propagate faster towards the west at lower latitudes. This westward propagation ranges between 0 to $4 \, \mathrm{cm \, s^{-1}}$ on average. The close agreement between the latitudinal means of c_x provides evidence that on average, TRAPs

295   move along with mesoscale eddies. We find similar coincidence for the latitudinal and longitudinal distribution of both zonal and meridional propagation speeds c_x and c_y, see Fig. A1. However, we find that mesoscale eddies exhibit more extreme propagation speeds, suggesting that eddies might only create persistent strain within a specific dynamic range or a specific combination of eddies.
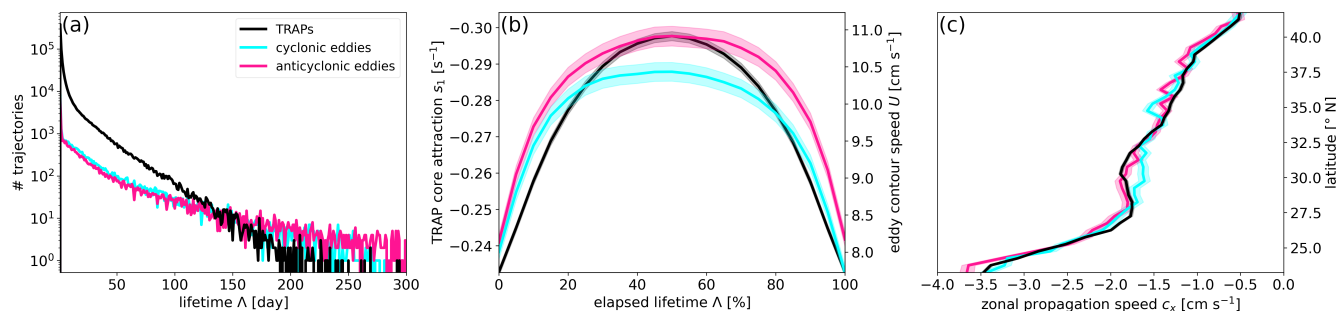
Figure 5. Comparisons between TRAPs and mesoscale eddies. (a) Disribution of lifetime Λ over all TRAP trajectories, cyclonic and anticyclonic eddy trajectories in the domain. The distributions of eddy lifetimes are cut off at 300 days for clarity. (b) Evolution of attraction rate s_1 over TRAP lifetime and contour speed U over eddy lifetime for phenomena with lifetimes $\Lambda > 30\,\mathrm{days}$. (c) Latitudinal dependence of zonal propagation speed c_x for 2,951,028 TRAP, 604,296 cyclonic and 608,650 anticyclonic eddy instances. Lines in (b) and (c) indicate bin means, shaded bands their errors w.r.t. a confidence level of 95%. Mesoscale eddies as detected by AVISO+ et al. (2022).

Our results indicate that TRAPs are certainly located within the mesoscale eddy field, but we wonder where exactly. While TRAPs exert maximum normal attraction and induce significant deformation, i.e. strain-dominated regions, coherent eddies are characterised by water parcels rotating about a common axis and closed transport barriers. Hence coherent eddies represent vorticity-dominated regions which should exclude TRAPs. As a consequence TRAPs should emerge at the eddy periphery. However, we find that the eddy detections from AVISO+ et al. (2022) are not able to explain all TRAP occurrences. We often find TRAPs at eddy boundaries, but we also frequenlty observe TRAPs in regions with no eddy detections or even inside eddy contours, see Fig. A2 or Video SV3 for details. The latter occurs for 15% of all TRAP detections and suggests the presence of multiple eddies within one eddy detection. Even though the eddy dataset allows us to reveal average relations between TRAPs and mesoscale eddies, it is not suited to describe the actual dynamics around individual TRAPs. Instead, we use the relative vorticity field to characterise the flow around TRAPs.

3.3 Vorticity patterns around TRAPs

A considerable number of TRAPs seems to be surrounded by four vortices of alternating polarity which exhibit perpendicular flow towards the TRAP core and tangential flow away from it w.r.t. the TRAP curve. We call this pattern a *quadrupole*. Here we unravel this quadrupole and variations of it to demonstrate the driving mechanisms behind the formation of mesoscale TRAPs. We compute the vorticity curves $\zeta(\alpha)$ around all available TRAPs and normalise each by its maximum absolute value to obtain $\hat{\zeta}(\alpha)$. First, we take this large ensemble of curves and show its mean and standard deviation in Fig. 6. This reveals the mean pattern in the vorticity field around a TRAP.
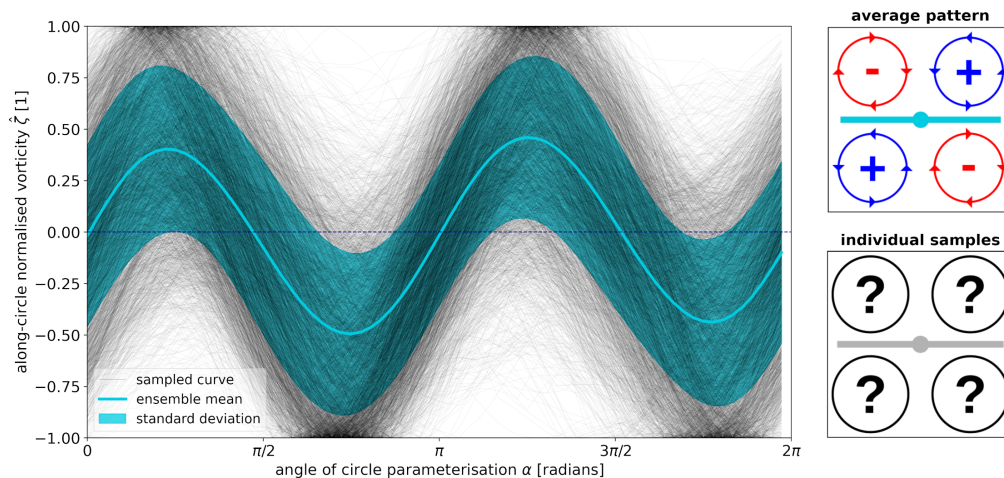
Figure 6. Ensemble of 3,568,850 vorticity curves $\hat{\zeta}(\alpha)$ around TRAPs. Every curve $\zeta(\alpha)$ is normalised by its maximum absolute value. $\hat{\zeta} > 0$ indicates cyclonic, $\hat{\zeta} < 0$ anticyclonic rotation in the surrounding flow field of a TRAP. The blue line indicates the ensemble mean, the shaded band its standard deviation. Black lines represent an arbitrary 0.1% subset from this ensemble. The panels on the right sketch two TRAPs, one surrounded by a quadrupole as it can be interpreted from the ensemble mean, the other surrounded by vortices of unknown polarity: What vorticity patterns will appear around individual samples?

The ensemble of all vorticity curves clearly resembles a sine wave. The similarity between the ensemble mean and a harmonic function as well as its smoothness is remarkable. Even though individual curves might not follow this shape, the entirety of the approx. 3.5 million curves generates a robust signal. Since a vorticity curve with four zero crossings and a polarity pattern of cyclonic, anticyclonic, cyclonic, anticyclonic sequence indicates a quadrupole, the above signal gives reason to believe that

320   the mean pattern in the vorticity field around a TRAP is a quadrupole. Figure 3 illustrates such a typical quadrupole situation.

We then remove the background vorticity from each vorticity curve and filter the ensemble of all vorticity curves $\zeta(\alpha)$ for the 10 distinct vortex combinations. The quadrupole pattern in Fig. 6 serves as our reference pattern and we define the other nine patterns in terms of variation from it. Therefore, we introduce the *quadrupole order* q. It describes the number of vortices in a given pattern that need to change polarity in order to obtain the reference quadrupole pattern. We group the vorticity patterns

325   of all the above 3,568,850 TRAP instances by q and illustrate the most frequent groups in Fig. 7, see Fig. S2 for more details on all 10 vorticity patterns and their attributed quadrupole order.
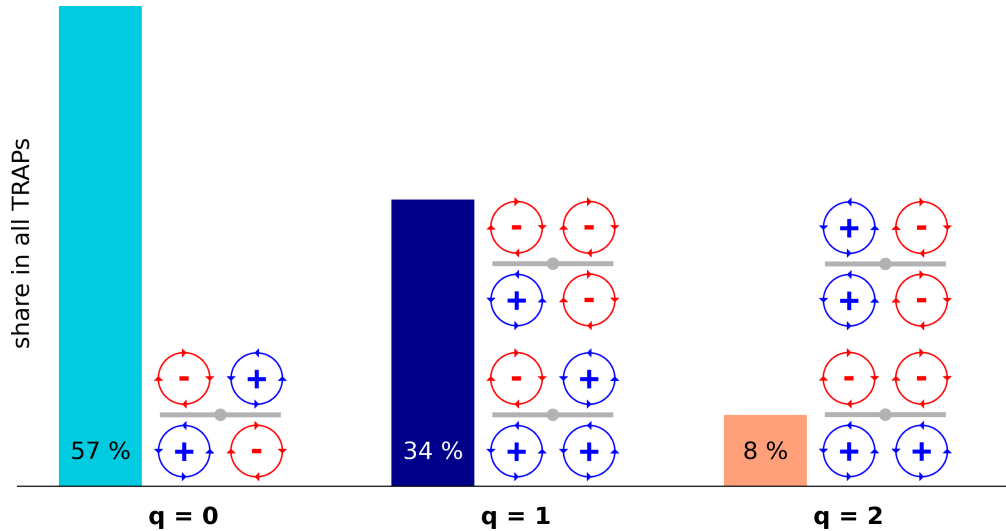
Figure 7. Quadrupole orders and their frequency. The quadrupole order q describes the number of vortices in a given pattern that need to change polarity in order to obtain the reference quadrupole pattern. After removing the background vorticity from every vorticity curve $\hat{\zeta}(\alpha)$, 99.97% of the ensemble can be explained by the five patterns illustrated here. Figure S2 provides an overview on all vorticity patterns.

We shorthand name TRAP instances within a specific quadrupole surrounding *q-th order quadrupoles*. Zero, first and second order quadrupoles constitute 99.97% of the signal in Fig. 6. We identify approx. 57% of all TRAPs as zero order quadrupoles,

330   34% as first order quadrupoles and 8% as second order quadrupoles. As we expect, the most prevalent group is the reference quadrupole indicated by the ensemble mean. However, a significant share of TRAPs is also surrounded by first order quadrupoles. A quick look into the ensemble means in Fig. S2 reveals that first order quadrupoles can also include dipoles with one dominating polarity and some second order quadrupoles might represent symmetric dipoles. Higher order quadrupoles also exist and involve the lowest attraction rates, but we neglect them since they rarely occur.

335

We now want to know how quadrupole patterns evolve over the TRAP lifetime Λ and how they relate to the attraction rate s_1. Panel (a) in Fig. 8 illustrates the shares of quadrupole orders zero, one and two at different evolution stages of long-living TRAPs. We observe a gradual change in the vorticity field around long-living TRAPs towards the reference quadrupole state during the first half of a life cycle, and away from the reference quadrupole state during the second half. Zero order quadrupoles

340   are the most important vortex group throughout the entire lifetime and they are especially abundant during the mature phase of TRAPs, i.e. between 20% and 80% of lifetime. However, the first order quadrupole is also a likely state at the formation and decay phase of this cycle.

A comparison between Figs. 8a and 5b suggests that the evolutions of quadrupole order q and TRAP attraction rate s_1 go

345   along with each other, i.e. TRAPs intensify towards their mid-life while their vorticity surroundings approach a lower order quadrupole state. From this we expect that zero, first and second order quadrupoles create different kinds of strain. Panel (b) in

Fig. 8 displays the distributions of the instantaneous attraction rates s_1 w.r.t. these quadrupole orders. The weakest TRAPs, i.e. with the largest strain rates s_1, are only surrounded by first order quadrupoles. Zero and second order quadrupole environments appear for slightly higher attractions, i.e. smaller values of s_1. All three distributions peak within the same niche but with
350 decreasing attraction rate, the probability density for second and first order quadrupoles decline faster than for the reference quadrupole. It shows that the probability to find strongly attracting TRAPs is higher among quadrupoles of order zero. The average attraction rates $\overline{s}_1$ confirm this tendency, the p-values for the respective differences in mean values result in $p < 0.001$. However, the strongest TRAPs are attributed to both the zero and first order quadrupole environments and in panel (b) we are looking at slight differences at the very extremes. Therefore we conclude that there is a trend towards the reference quadrupole
355 environment for increasingly attractive TRAPs. Nevertheless, first order quadrupoles are likewise able to induce high strain. We now investigate which of these groups organises tracer patterns particularly well.
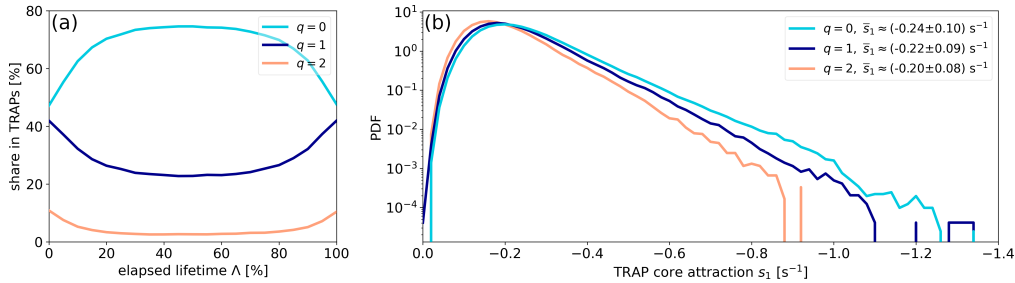
Figure 8. Distribution of quadrupole orders over TRAP lifetime and attraction. (a) Shares of zero, first and second order quadrupoles over the lifetime of 26,675 long-living TRAPs with $\Lambda > 30\,\mathrm{days}$. (b) Distribution of TRAP attraction rates s_1 for zero, first and second order quadrupoles.

3.4 Impact on drifters

We identify 33.878 drifter-TRAP pairs with retention times of $\varphi > 1\,\mathrm{day}$. These pairs cover 73% of all drifter days and exhibit a mean retention time of $\overline{\varphi} \approx (4.8 \pm 3.7)\,\mathrm{days}$ which reflects the transient impact of TRAPs, i.e. drifters are accumulated and
360 dispersed again within a few days. However, we also find a few drifters that spend multiple weeks around a TRAP. The highest retention time we measure counts $\varphi = 46\,\mathrm{days}$. Pairs with retention times $\varphi > 7\,\mathrm{days}$ represent only 9% of all pairs but cover 28% of all drifter days. In general, we observe similar behaviours of drogued and undrogued drifters around TRAPs, but we emphasise a subtle difference in retention times to explain why we find 2.6 times more undrogued than drogued drifter-TRAP pairs while there are only 1.6 times more undrogued than drogued drifters in our domain. Figure 9 presents the distribution
365 of retention times φ over these drifter-TRAP pairs w.r.t. a pair's drogue state. The probability density function illustrates, irrespective of sample size, which drogue type is more likely to enter into long retention. With increasing retention time φ, the probability density for undrogued drifters declines faster than for drogued ones. In general, drogued drifters show a higher susceptibility to stay around TRAPs for 8 days and longer. A longer retention of drogued drifters eventually makes them less available for transient pairings.
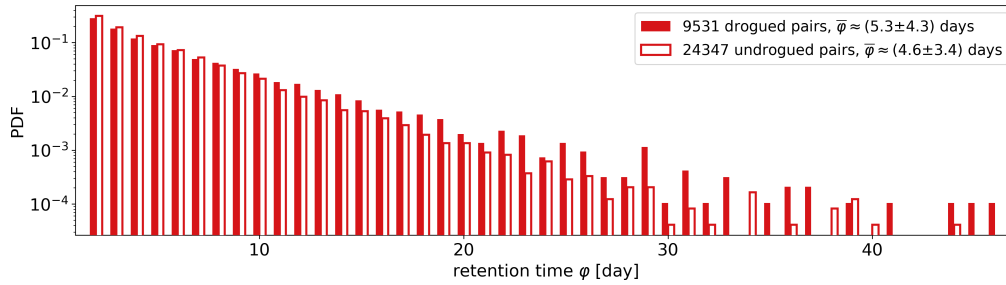
Figure 9. Retention times of drifters around TRAPs. Probability density function of retention times φ with respect to a drifter's drogue type. Drogued drifters remain on average $\overline{\varphi} \approx (5.3 \pm 4.3)$ days, undrogued ones $\overline{\varphi} \approx (4.6 \pm 3.4)$ days around a TRAP. The p-value for the difference in means results in p < 0.001. Pairs with retention times of 1 day are excluded.

370   We study the average drifter motion around TRAPs and find that transport patterns depend on the evolution stage of the respective TRAP. Thus we divide all drifter-TRAP pairs into four groups. The first group includes pairs for which the respective TRAP forms and decays during the drifter visit. Technically, this means that a pair includes the first and last detection of a TRAP. The second group consists of pairs which occur during the formation of a TRAP but end before its decay. The third group entails pairs which begin after the formation of a TRAP but end with its decay. And the fourth group defines pairs that 375   exist throughout the lifetime of a TRAP but exclude its formation and decay. Table 1 summarises the average retention times, attraction rates and TRAP lifetimes related to these groups. We find the longest average retention time for pairs that occur throughout the life cycle of a TRAP without formation or decay. These pairs show to involve TRAPs of significantly stronger attraction and higher persistency compared to pairs that occur during TRAP formation and/or decay.

Table 1. Characteristics of drifter-TRAP pairs at specific TRAP evolution stages. $\overline{\varphi}$ indicates the average retention times over all respective pairs, $\overline{\Lambda}$ the average lifetime over all associated TRAPs and $\overline{s}_1$ the average attraction rate over all associated TRAP instances. TRAP formation is given if a pair includes the first detection of a TRAP, TRAP decay if a pair includes the last detection.

	TRAP formation	TRAP decay	$\overline{\varphi}$ [days]	$\overline{\Lambda}$ [days]	$\overline{s}_1$ [s^{-1}]	# pairs	share in drifter days
Group I	yes	yes	(3.5 ± 2.6)	(3.5 ± 2.6)	(-0.17 ± 0.07)	5456	8.5%
Group II	yes	no	(4.8 ± 3.8)	(19.6 ± 20.8)	(-0.21 ± 0.08)	5521	11.8%
Group III	no	yes	(4.7 ± 3.7)	(19.6 ± 20.3)	(-0.21 ± 0.08)	5609	11.8%
Group IV	no	no	(5.3 ± 3.8)	(47.9 ± 35.4)	(-0.27 ± 0.11)	17292	40.9%

     In Fig. 10 we illustrate the average drifter motion around TRAPs with respect to this grouping. We rotate drifter tracks 380   around TRAPs towards the zonal axis and allocate their respective drifter positions to hexagonal bins. For every bin, we average the elapsed retention time φ and the eastward and northward velocity components over all binned drifter positions. Bin colours indicate the average elapsed retention time φ per bin, quivers the average velocity components.

Panel (a) highlights the average drifter motion around TRAPs that form and decay. The situation appears rather chaotic
385   with no specific motion pattern to detect. Velocity quivers hardly show any preferred direction of transport and green colours
dominate the picture. The colour map indicates that the retention times of the underlying drifter-TRAP pairs begin and end
anywhere throughout the search circle. Panel (b) gives insight into drifter motion during the formation of TRAPs which overlast
the retention time. We find that drifters are majorly transported away from the TRAP and in parallel to the TRAP curve. Panel
(c) describes the opposite situation in which decaying TRAPs rather attract than disperse drifters. This attraction is generally
390   directed towards the TRAP core. Panels (a) to (c) reveal that drifters around TRAPs that either form and/or decay do not tend to
follow a hyperbolic pattern. But TRAPs that are at a final stage of their life cycle can at least indicate the confluence of material.

In contrast, the velocity quivers in panel (d) where TRAP formation and decay are excluded describe hyperbolic transport
as expected, i.e. drifters flow perpendicularly towards the TRAP core and tangentially away from it, with respect to the TRAP
395   curve. We also observe distinct regions of light blue and red bin colours which indicate that many drifters enter the zone per-
pendicular towards the TRAP and leave it at one end of the structure. A comparison with Figs. 5b, 8a and Table 1 clarifies that
hyperbolic transport primarily occurs throughout the mature phase of a long-living TRAP because at this stage, the surrounding
flow is particularly organised into a quadrupole pattern that generates high strain.
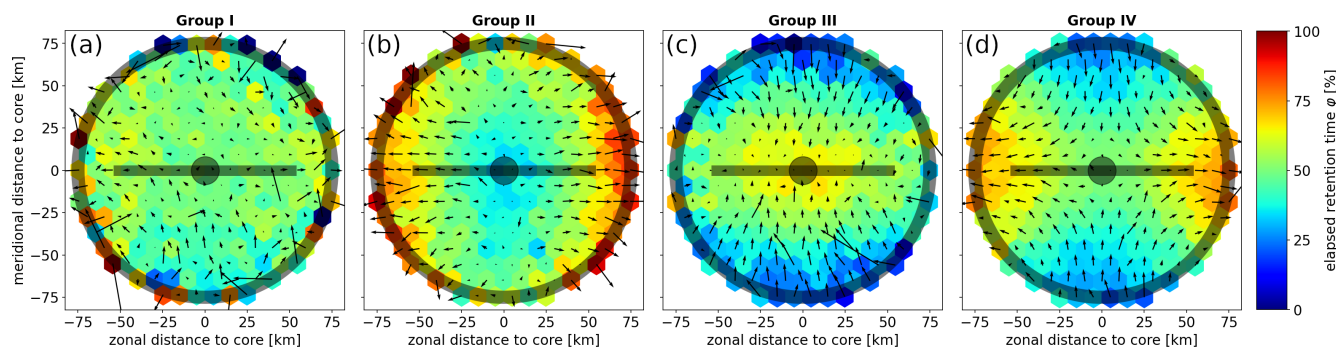
Figure 10. Drifter motion around TRAPs. For every drifter-TRAP pair, we determine the angle between the longer branch of the first TRAP
instance and the zonal axis with 0° pointing eastward and angles increasing counterclockwise. We use this angle to rotate all drifter positions
towards the zonal axis. We allocate all rotated drifter positions to hexagonal bins and for every bin, we average the elapsed retention time φ
as well as the eastward and northward velocity components over all binned drifter instances. The colour mapping indicates bin averages of
φ, quivers the average velocity components. A transparent TRAP in the middle indicates a generic profile, a black circle the limits of the
drifter search zone around it. (a) TRAP forms and decays, (b) TRAP only forms, (c) TRAP only decays and (d) TRAP neither forms nor
decays during the drifter visit.

4 Summary, discussion and conclusion

400 We studied the characteristics of TRAPs and the prospects for predicting debris transport from this mesoscale permitting dataset. Our findings provide an advanced understanding of TRAPs in the Great Pacific Garbage Patch and demonstrate the importance of TRAP lifetime estimations to an operational application. We find that the life cycle of TRAPs can range from days to seasons with an average lifetime of $\overline{\Lambda} \approx (6 \pm 12)$ days. However, 41% of all TRAP detections relate to profiles with lifetimes of $\Lambda > 30$ days. Such long-living TRAPs exhibit a distinct evolution of attraction strength, they intensify during the

405 first and weaken during the second half of their life cycle. At the same time, the vorticity field around TRAPs gradually changes towards and away from a particularly ordered state, i.e. a group of four vortices with alternating polarity. Therefore, the life cycle of TRAPs can explain why we observe hyperbolic drifter transport primarily throughout the mature phase of long-living TRAPs. At this stage, the surrounding flow is particularly organised and generates high strain. We find that hyperbolic transport around TRAPs takes on average $\overline{\varphi} \approx (5.3 \pm 3.8)$ days but also detect drifters that spend multiple weeks around a TRAP. The

410 highest retention time we measure counts $\varphi = 46$ days.

We identify the evolution stage of TRAPs as the most significant predictor for drifter motion. But the coherence of surrounding vortices might further explain our observations of hyperbolic transport and long retentions. We propose to investigate this with higher-resolution measurements of the flow which can resolve the small-scale vortices that we see around many TRAPs

415 in SV3. The mesoscale eddy detections by AVISO+ et al. (2022) neither capture such vortices at the limit between the meso- and submesoscale which reflects in the high number of TRAPs without close-by eddy detections. Moreover, we find 15% of all TRAPs inside these eddy detections although coherent eddies should exclude strain-dominated regions. It is known that eddy detection algorithms based on closed contours of sea surface height often yield false-positive identifications (Beron-Vera et al., 2013; Andrade-Canto and Beron-Vera, 2022). Liu and Abernathey (2023) present an alternative algorithm which detects

420 eddies from Lagrangian-averaged vorticity deviations (LAVD, Haller et al. (2016)). They claim the absence of false positive detections, however, we still find TRAPs that intersect these eddy detections, possibly due to the discrepancy between the time-scale over which Lagrangian averaging takes place and the instantaneous nature of TRAPs, see Fig. A2 for details. We expect true coherence and no inclusion of TRAPs when we use a detection framework that descends from the deformation tensor $\mathbf{S}(\boldsymbol{x},t)$. Serra and Haller (2016) introduce elliptic OECSs which can be derived from singularities of $\mathbf{S}(\boldsymbol{x},t)$ and build

425 a complement to the strain-dominated regions uncovered by TRAPs, with the additional benefit of both computations being instantaneous. A computational implementation of elliptic OECSs would be subject to future research.

There is an ongoing debate on whether mesoscale eddies accumulate and transport floating material. van Sebille et al. (2020) discuss confirming examples such as Brach et al. (2018), Budyansky et al. (2015) and Dong et al. (2014) while Abernathey

430 and Haller (2018) and Wang et al. (2015) show that transport by coherent eddies is negligible. This controversy rises from the use of different concepts to identify eddy boundaries. Abernathey and Haller (2018) find that material transport is caused by stirring and filamentation at the periphery of strictly coherent eddies, rather than by the coherent motion within eddy cores.

They emphasise the lack of objective methods to identify such peripheral regions. But TRAPs describe the limit between eddy peripheries and should be able to contribute to this investigation. We find that on large time scales, there is no preference of
435   drifter positions around TRAPs or within eddy boundaries defined by AVISO+ et al. (2022). The share of drifter days spent around TRAPs or within eddies approx. equals the proportion of surface area that is covered by these structures. However, there are temporary preferences on short time scales which motivate a follow-up analysis, see the time series in Fig. S3 for details.

440   There are obvious limits to the application of this mesoscale permitting dataset. The effective resolution in space and time can be expected to be greater than the 0.25° latitude-longitude grid and the daily frequency. We observe effects of this in animations where TRAPs reappear after a one-day gap. At such a gap, our tracking algorithm defines a new trajectory and therefore TRAP lifetimes might be underestimated. In a similar way, detection gaps affect the identification of drifter-TRAP pairs, leading to an underestimation of retention times. Nevertheless, we find a remarkable consistency between Duran et al.
445   (2021) and our study. They find persistent mesoscale TRAPs that predict the spread of surface oil at least eight days in advance and confirm our finding of retention times of $\varphi = (5.3 \pm 3.8)$ days for hyperbolic drifter motion. The agreement between their study and ours, as well as the overall similar behaviour we observe for drogued and undrogued drifters, further underlines the concept's robustness against differences in tracer properties.

450   Even though our study cannot resolve important submesoscale processes like e.g. filamentation, Langmuir cells or submesoscale vortices, it demonstrates the capability of TRAPs to predict material transport from first order mesoscale observations. Our algorithms offer a great chance to reapply the TRAPs concept to future high-resolution observations that will be provided by the current SWOT mission (International Altimetry Team, 2021). An interesting approach would be to study the flow around drifter-TRAP pairs with long retention times. These long retention times might be due to drifter trapping within submesoscale
455   vortices and filaments that result from instabilities at mesoscale fronts (van Sebille et al., 2020; Zhang et al., 2019). Mesoscale TRAPs indicate these mesoscale fronts and might provide a window to enhanced material clustering at the submesoscale. We propose to recast our TRAPs record (Kunz, 2024b) for periods with available SWOT measurements to investigate whether TRAPs can indicate material accumulation at operational scales $\mathcal{O}(1-10\mathrm{km})$ but from large-scale observations of sea surface height $\mathcal{O}(10-100\mathrm{km})$, even if the geostrophic assumption is needed to obtain a sea-surface velocity from SWOT measure-
460   ments. Such exploration can be complemented with additional observations in coastal regions from high-frequency radar which gives the full and not only the geostrophic sea-surface velocity.

Our results can already support offshore cleanup operations since they reveal which TRAPs are most likely to indicate large-scale confluence of drifting objects. Operators should search for long-living TRAPs that are at an advanced stage of
465   their life cycle. These TRAPs streamline floating objects into hyperbolic pathways. Such a streamlined bypass involves a short but strong attraction which could be exploited to *filter* the flow around a TRAP. But we also find TRAPs that retain material over multiple weeks. These long-term retentions can start at any stage of a TRAP's life cycle and drifters remain closer to the

TRAP core than for streamlined bypasses. An investigation of the conditions causing this behaviour could further improve the prospects of a cleanup operation, especially since long retentions of $\varphi > 7\,\mathrm{days}$ are rare but cover up to 28% of all drifter days.

470 And this research is not limited to the subject of marine debris. Our findings may also benefit other challenges like e.g. optimal drifter deployment, sargassum removal, the identification of foraging hotspots or search and rescue.

Appendix A: Figures
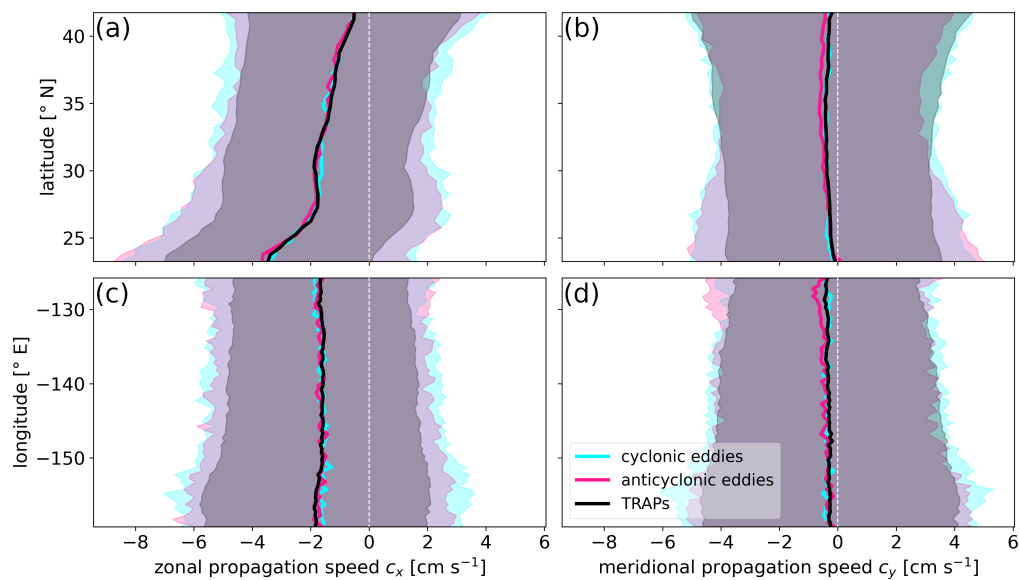
Figure A1. Comparison of propagation speeds between TRAPs and mesoscale eddies. Latitudinal dependence of the (a) zonal propagation speed c_x and (b) meridional propagation speed c_y. Longitudinal dependence of the (c) zonal propagation speed c_x and (d) meridional propagation speed c_y. Lines indicate bin means, shaded bands the respective standard deviations from 2,951,028 TRAP, 604,296 cyclonic and 608,650 anticyclonic eddy instances. Mesoscale eddies as detected by AVISO+ et al. (2022).
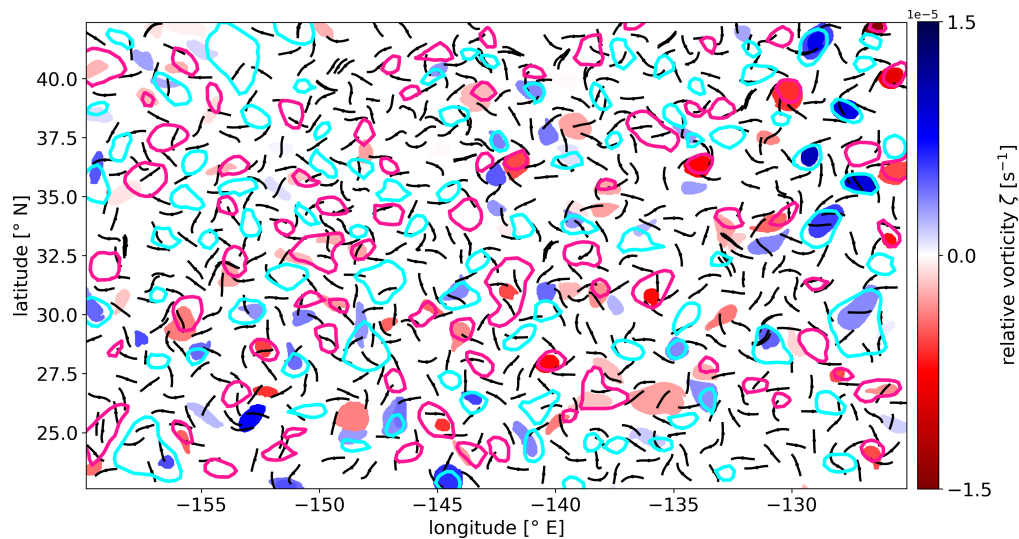
Figure A2. Snapshot of mesoscale TRAPs and mesoscale eddy detections within the study domain. Black lines represent TRAPs. Cyan/pink lines depict the speed contours of cyclonic/anticyclonic mesoscale eddies as detected by AVISO+ et al. (2022). Blue/red patches depict Lagrangian particles trapped by cyclonic/anticyclonic coherent eddy boundaries as detected by Liu and Abernathey (2022) for the same snapshot. The colour scale on the right indicates the relative vorticity ζ of Lagrangian particles.

Appendix B: Tables

Table B1. Benefits of TRAPs. Adopted from Serra and Haller (2016), Serra et al. (2020) and Duran et al. (2021).

use velocity snapshots	TRAPs can be directly inferred from snapshots of the surface velocity field and thus are light in computation. They allow for input data with time gaps and predictions can be made from a nowcast of the velocity field.
avoid pitfalls of trajectory integration	TRAPs do not require costly trajectory integrations, tracer release times, locations or the length of the observation period. Velocity errors do not accumulate which should make TRAPs less sensitive to uncertainties in the underlying velocity field. They also provide full domain coverage while Lagrangian methods become computationally demanding with increasing resolution of the initial particle field where particles may eventually leave a finite-size domain.
indicate direction of transport	What makes TRAPs special is that they indicate the directions of transport while other structures like e.g. s_1 minima, divergence minima or ridges of the Finite-Time Lyapunov Exponent (FTLE) field don't. FTLE ridges do not necessarily indicate the direction of largest stretching (Haller, 2015).
easy to interpret	TRAPs describe localised, one-dimensional curves of attraction in contrast to large open sets of e.g. horizontal divergence or particle density.
robust	TRAPs are robust to different inertia and windage effects and thus are insensitive to varying shape or submergence level of drifting objects.
uncover hidden flow structures	TRAPs can be perpendicular to streamlines and exist in divergence-free flows.
observer-independent	The objective nature of TRAPs leads to the same conclusions on different platforms. Classic Eulerian quantities like streamlines, velocity magnitude, velocity gradient, energy, relative vorticity are not objective and will lead to different results in different frames of reference.
scale-invariant	TRAPs can be computed for velocity fields of any temporal and spatial resolution. The concept can be applied to the scales of the confluence phenomena of interest.

Table B2. Algorithm to compute Transient Attracting Profiles in a two-dimensional flow. Adopted from Serra and Haller (2016) and Serra et al. (2020).

Input: A two-dimensional Eulerian velocity field $\boldsymbol{u}(\boldsymbol{x}, t)$

Compute

1. the rate-of-strain tensor $\mathbf{S}(\boldsymbol{x}, t) = \frac{1}{2}(\boldsymbol{\nabla}\boldsymbol{u}(\boldsymbol{x}, t) + [\boldsymbol{\nabla}\boldsymbol{u}(\boldsymbol{x}, t)]^{\top})$

   at the current time t on a rectangular grid over the (x_1, x_2) coordinates.

2. the eigenvalue fields $s_1(\boldsymbol{x}, t) \leq s_2(\boldsymbol{x}, t)$ and the associated unit eigenvector fields $\boldsymbol{e}_i(\boldsymbol{x}, t)$ of $\mathbf{S}(\boldsymbol{x}, t)$ for $i = 1, 2$.

3. the set $S_{1m}(t)$ of negative local minima of $s_1(\boldsymbol{x}, t)$.

4. TRAPs ($\boldsymbol{e}_2$-lines) as solutions of the ODE

$$
\begin{cases}
\dfrac{d\boldsymbol{x}}{ds} = \text{sign}\langle \boldsymbol{e}_2(\boldsymbol{x}(s)), \boldsymbol{e}_2(\boldsymbol{x}(s - \Delta)) \rangle \boldsymbol{e}_2(\boldsymbol{x}(s)) \\
\boldsymbol{x}(0) \in S_{1m}(t).
\end{cases}
$$

where s is the independent variable of the TRAP curve parameterisation $\boldsymbol{x}(s)$, Δ denotes the integration step in the arclength parameter s and $\boldsymbol{x}(0)$ indicates the position of a TRAP core. The sign term in step 4 guarantees the local smoothness of the direction field $\boldsymbol{e}_2$. Stop integration when $s_1(\boldsymbol{x}(s))$ ceases to be montone increasing or when $s_1(\boldsymbol{x}(s)) > 0.3 \cdot s_1(\boldsymbol{x}(0))$. TRAP curves are shortened such that the attraction rate along the curve is everywhere at least 30% of the attraction at the respective core in order to ensure that TRAPs indicate a distinguished attraction relative to nearby structures (Serra et al., 2020).

Output: Transient Attracting Profiles at time t and their normal attraction rate field $s_1(\boldsymbol{x}, t)$.

Code and data availability. We provide source code at Kunz (2024a) to post-process TRAP computations, to track TRAPs through the
domain and to identify drifter-TRAP pairs. We further provide a 20-years dataset of TRAP detections with lifetime estimations and vorticity
pattern detections and our dataset of drifter-TRAP pair detections at Kunz (2024b).

Video supplement. We provide animations of the TRAPs tracking algorithm in SV1, of the evolution of TRAPs, drifter positions and the
relative vorticity field in SV2 and of the evolution of TRAPs, mesoscale eddy detections and the relative vorticity field in SV3. SV1, SV2
and SV3 are available at Kunz (2024c) and Fig. S4 summarises the details.

Author contributions. LK programmed the algorithms, did the analyses and wrote much of the text. AG supervised the writing process,
contributed to interpreting the results and wrote text. AG and CE acquired the funding. CE contributed to editing the paper, interpreting the
results and wrote text. RD contributed to developing the methodology, editing, interpretation of results and wrote text. BSR contributed to
methodology, interpretation and acquired computational resources. All authors contributed to the design of the experiment.

Competing interests. The authors declare that they have no conflict of interest.

Acknowledgements. This paper is a contribution to the project L3 (Meso- to submesoscale turbulence in the ocean) of the Collaborative
Research Centre TRR 181 "Energy Transfer in Atmosphere and Ocean" funded by the German Research Foundation (DFG) and has been
written in collaboration with The Ocean Cleanup.

References

Abernathey, R. and Haller, G.: Transport by Lagrangian Vortices in the Eastern Pacific, Journal of Physical Oceanography, 48, 667–685, https://doi.org/10.1175/JPO-D-17-0102.1, 2018.

Andrade-Canto, F. and Beron-Vera, F. J.: Do Eddies Connect the Tropical Atlantic Ocean and the Gulf of Mexico?, Geophysical Research Letters, 49, e2022GL099 637, https://doi.org/10.1029/2022GL099637, 2022.

AVISO+, CNES, SSALTO/DUACS, and IMEDEA: Mesoscale Eddy Trajectories Atlas 3.2 Delayed-Time (META3.2 DT) Allsat Version, https://doi.org/10.24400/527896/a01-2022.005.220209, 2022.

Beron-Vera, F. J., Wang, Y., Olascoaga, M. J., Goni, G. J., and Haller, G.: Objective Detection of Oceanic Eddies and the Agulhas Leakage, Journal of Physical Oceanography, 43, 1426 – 1438, https://doi.org/10.1175/JPO-D-12-0171.1, 2013.

Brach, L., Deixonne, P., Bernard, M.-F., Durand, E., Desjean, M.-C., Perez, E., van Sebille, E., and ter Halle, A.: Anticyclonic eddies increase accumulation of microplastic in the North Atlantic subtropical gyre, Marine Pollution Bulletin, 126, 191–196, https://doi.org/10.1016/j.marpolbul.2017.10.077, 2018.

Budyansky, M., Goryachev, V., Kaplunenko, D., Lobanov, V., Prants, S., Sergeev, A., Shlyk, N., and Uleysky, M.: Role of mesoscale eddies in transport of Fukushima-derived cesium isotopes in the ocean, Deep Sea Research Part I: Oceanographic Research Papers, 96, 15–27, https://doi.org/10.1016/j.dsr.2014.09.007, 2015.

Chelton, D. B., Schlax, M. G., and Samelson, R. M.: Global observations of nonlinear mesoscale eddies, Progress in Oceanography, 91, 167–216, https://doi.org/10.1016/j.pocean.2011.01.002, 2011.

CMEMS: Global Total Surface and 15m Current (COPERNICUS-GLOBCURRENT) from Altimetric Geostrophic Current and Modeled Ekman Current Reprocessing, https://doi.org/10.48670/moi-00050, 2022a.

CMEMS: Global Ocean Gridded L 4 Sea Surface Heights And Derived Variables Reprocessed 1993 Ongoing, https://doi.org/10.48670/moi-00148, 2022b.

Dong, C., McWilliams, J., Liu, Y., and Chen, D.: Global heat and salt transports by eddy movement, Nature communications, 5, 3294, https://doi.org/10.1038/ncomms4294, 2014.

Duran, R., Nordam, T., Serra, M., and Barker, C.: Horizontal transport in oil-spill modeling, pp. 59–96, Elsevier, https://doi.org/10.1016/B978-0-12-819354-9.00004-1, https://arxiv.org/abs/2009.12954, 2021.

Haller, G.: Lagrangian Coherent Structures, Annual Review of Fluid Mechanics, 47, 137–162, https://doi.org/10.1146/annurev-fluid-010313-141322, 2015.

Haller, G., Hadjighasem, A., Farazmand, M., and Huhn, F.: Defining coherent vortices objectively from the vorticity, Journal of Fluid Mechanics, 795, 136–173, https://doi.org/10.1017/jfm.2016.151, 2016.

International Altimetry Team: Altimetry for the future: Building on 25 years of progress, Advances in Space Research, 68, 319–363, https://doi.org/10.1016/j.asr.2021.01.022, 25 Years of Progress in Radar Altimetry, 2021.

Kunz, L.: Track and analyse Transient Attracting Profiles in the Great Pacific Garbage Patch, https://github.com/kunzluca/trapsgpgp, 2024a.

Kunz, L.: Datasets to Transient Attracting Profiles in the Great Pacific Garbage Patch, https://doi.org/10.5281/zenodo.10993736, 2024b.

Kunz, L.: Supplementary Videos to Transient Attracting Profiles in the Great Pacific Garbage Patch, https://doi.org/10.5281/zenodo.10943728, 2024c.

Law, K. L., Morét-Ferguson, S. E., Goodwin, D. S., Zettler, E. R., DeForce, E., Kukulka, T., and Proskurowski, G.: Distribution of Surface Plastic Debris in the Eastern Pacific Ocean from an 11-Year Data Set, Environmental Science & Technology, 48, 4732–4738, https://doi.org/10.1021/es4053076, 2014.

Lebreton, L., Slat, B., Ferrari, F., Sainte-Rose, B., Aitken, J., Marthouse, R., Hajbane, S., Cunsolo, S., Schwarz, A., Levivier, A., et al.: Evidence that the Great Pacific Garbage Patch is rapidly accumulating plastic, Scientific reports, 8, 1–15, https://doi.org/10.1038/s41598-018-22939-w, 2018.

Lindo-Atichati, D., Jia, Y., Wren, J. L. K., Antoniades, A., and Kobayashi, D. R.: Eddies in the Hawaiian Archipelago Region: Formation, Characterization, and Potential Implications on Larval Retention of Reef Fish, Journal of Geophysical Research: Oceans, 125, e2019JC015 348, https://doi.org/10.1029/2019JC015348, 2020.

Liu, T. and Abernathey, R.: A global Lagrangian eddy dataset based on satellite altimetry (GLED v1.0), https://doi.org/10.5281/zenodo.7349753, last access: 22 April 2024, 2022.

Liu, T. and Abernathey, R.: A global Lagrangian eddy dataset based on satellite altimetry, Earth System Science Data, 15, 1765–1778, https://doi.org/10.5194/essd-15-1765-2023, 2023.

Lumpkin, R. and Centurioni, L.: Global Drifter Program quality-controlled 6-hour interpolated data from ocean surface drifting buoys, https://doi.org/10.25921/7ntx-z961, last access: 15 December 2022, 2019.

Olbers, D., Willebrand, J., and Eden, C.: Ocean Dynamics, Springer Berlin Heidelberg, https://doi.org/10.1007/978-3-642-23450-7, 2012.

Onink, V., Wichmann, D., Delandmeter, P., and van Sebille, E.: The Role of Ekman Currents, Geostrophy, and Stokes Drift in the Accumulation of Floating Microplastic, Journal of Geophysical Research: Oceans, 124, 1474–1490, https://doi.org/10.1029/2018JC014547, 2019.

Pegliasco, C., Chaigneau, A., and Morrow, R.: Main eddy vertical structures observed in the four major Eastern Boundary Upwelling Systems, Journal of Geophysical Research: Oceans, 120, 6008–6033, https://doi.org/10.1002/2015JC010950, 2015.

Röhrs, J., Sutherland, G., Jeans, G., Bedington, M., Sperrevik, A. K., Dagestad, K.-F., Gusdal, Y., Mauritzen, C., Dale, A., and LaCasce, J. H.: Surface currents in operational oceanography: Key applications, mechanisms, and methods, Journal of Operational Oceanography, 0, 1–29, https://doi.org/10.1080/1755876X.2021.1903221, 2021.

Serra, M.: Compute Transient Attracting Profiles (TRAPs), https://github.com/MattiaSerra/TRAPs, last access: 15 December 2022, 2020.

Serra, M. and Haller, G.: Objective Eulerian coherent structures, Chaos: An Interdisciplinary Journal of Nonlinear Science, 26, 053 110, https://doi.org/10.1063/1.4951720, 2016.

Serra, M., Sathe, P., Rypina, I., Kirincich, A., Ross, S. D., Lermusiaux, P., Allen, A., Peacock, T., and Haller, G.: Search and rescue at sea aided by hidden flow structures, Nature Communications, 11, https://doi.org/10.1038/s41467-020-16281-x, 2020.

Slat, B.: First 100,000 KG Removed From the Great Pacific Garbage Patch, https://theoceancleanup.com/updates/first-100000-kg-removed-from-the-great-pacific-garbage-patch/, last access: 15 December 2022, 2022.

van Sebille, E., Griffies, S. M., Abernathey, R., Adams, T. P., Berloff, P., Biastoch, A., Blanke, B., Chassignet, E. P., Cheng, Y., Cotter, C. J., Deleersnijder, E., Döös, K., Drake, H. F., Drijfhout, S., Gary, S. F., Heemink, A. W., Kjellsson, J., Koszalka, I. M., Lange, M., Lique, C., MacGilchrist, G. A., Marsh, R., Mayorga Adame, C. G., McAdam, R., Nencioli, F., Paris, C. B., Piggott, M. D., Polton, J. A., Rühs, S., Shah, S. H., Thomas, M. D., Wang, J., Wolfram, P. J., Zanna, L., and Zika, J. D.: Lagrangian ocean analysis: Fundamentals and practices, Ocean Modelling, 121, 49–75, https://doi.org/10.1016/j.ocemod.2017.11.008, 2018.

van Sebille, E., Aliani, S., Law, K. L., Maximenko, N., Alsina, J. M., Bagaev, A., Bergmann, M., Chapron, B., Chubarenko, I.,
560   Cózar, A., et al.: The physical oceanography of the transport of floating marine debris, Environmental Research Letters, 15, 023 003,
https://doi.org/10.1088/1748-9326/ab6d7d, 2020.

Wang, Y., Olascoaga, M. J., and Beron-Vera, F. J.: Coherent water transport across the South Atlantic, Geophysical Research Letters, 42,
4072–4079, https://doi.org/10.1002/2015GL064089, 2015.

Zhang, Z., Qiu, B., Klein, P., and Travis, S.: The influence of geostrophic strain on oceanic ageostrophic motion and surface chlorophyll,
565   Nature Communications, 10, 2838, https://doi.org/10.1038/s41467-019-10883-w, 2019.